Original Paper

Eletrônica de Potência
Open Journal of Power Electronics

Received January 19, 2026; Received in revised form April 14, 2026, May 29, 2026; Accepted June 22, 2026; Date of publication June 26, 2026.
The review of this paper was arranged by Associate Editor Montiê A. Vitorino and Editor-in-Chief Allan F. Cupertino.
Digital Object Identifier http://doi.org/10.18618/REP.e202622

Efficiency Optimization of a Dual Active Bridge Converter with a Variable Inductor for Battery Charging Applications

Conrado G. Marques[1,2,*], João P. S. Cipriani[1,2], Leandro Roggia[2], Marina Perdigão[3], Jonas R. Tibola [2] and Álysson R. Seidel[1,2]

[1]Federal University of Santa Maria (UFSM), Electrical Engineering Post-Graduation Program, Santa Maria, Brazil
[2]Industrial Technical School of Santa Maria (CTISM - UFSM), Santa Maria, Brazil
[3]Polytechnic Institute of Coimbra, Coimbra, Portugal

conrado.gomes@ufsm.br*; jpcipriani@gmail.com; perdigao@isec.pt; roggia@ctism.ufsm.br; jrtibola@ctism.ufsm.br; seidel@ctism.ufsm.br.
*Corresponding author.

ABSTRACT This paper investigates the efficiency improvements achieved by using a Variable Inductor (VI) in a Dual Active Bridge (DAB) converter for battery charging applications. The introduction of the VI adds a degree of freedom to conventional Phase-Shift Modulation (PSM), which extends the soft-switching range under light-load conditions and reduces reactive power under high load conditions. However, an optimal combination of power transfer inductance (L_{DAB}) and phase-shift (PS) exists that yields maximum efficiency for each output power (P_o), and conversion ratio d. To validate this, a 600 W DAB converter prototype was experimentally developed. The efficiency results obtained from a sweep of L_{DAB} and PS were compared against those of a fixed-inductance DAB (FI-DAB). The experimental results demonstrate the superior performance of the proposed VI-DAB converter under both high and low load conditions.

KEYWORDS Circulating Energy, Phase-shift, Variable Inductor, Efficiency, DAB.

I. INTRODUCTION

The Dual-Active-Bridge (DAB) converter, originally proposed in [1], is widely implemented in applications requiring high power density, galvanic isolation, and bidirectional power transfer. Owing to its bidirectional capability, the DAB converter is extensively used in systems integrating battery energy storage (BESS) [2], including uninterruptible power supplies (UPS) [3], DC microgrids [4], ultra-fast electric vehicle (EV) charging stations [5], and vehicle-to-grid (V2G) applications [6].

Single-Phase-Shift (SPS) modulation [7] is the most widely adopted strategy for controlling DAB converters, owing to its simplicity and relatively high efficiency in practical implementations. It regulates power flow by adjusting the phase shift (PS) between the voltages of the two full-bridges. However, relying solely on PS as a control variable introduces limitations, especially under wide load variations and when the voltage conversion ratio (d) deviates from unity. In such scenarios, the converter loses Zero-Voltage Switching (ZVS) under light-load conditions. Conversely, at high-load conditions and for $d \neq 1$, significant circulating currents—analogous to reactive power—lead to increased conduction losses in power devices and elevated copper losses in the transformer windings [8].

To address these limitations, several approaches have been proposed that introduce additional degrees of freedom in the DAB converter. Among them, modulation strategies are the most widely reported, including Dual-Phase-Shift (DPS) [9], Triple-Phase-Shift (TPS) [10], and Extended-Phase-Shift (EPS) [11]. These approaches rely on the coordinated adjustment of multiple control variables, such as the duty cycles of the primary and secondary bridges and the PS, in order to improve efficiency. However, their performance strongly depends on the identification of optimal control parameter combinations.

Although modulation approaches do not require additional hardware, they significantly increase system complexity. This is mainly due to the multiple switching modes involved, which require piecewise mathematical models and complicate both control design and the analytical evaluation of performance metrics such as RMS current and reactive power [12]–[14]. Furthermore, the presence of multiple control variables leads to a multi-dimensional optimization problem, whose real-time implementation can be challenging for conventional microcontrollers. In practice, this often requires precomputed look-up tables (LUTs) or advanced optimization and control techniques, such as Particle Swarm Optimization (PSO) [12], Karush–Kuhn–Tucker (KKT) conditions [15], Model Predictive Control (MPC) [16], [17],

and Model Reference Adaptive Control (MRAC) [18], which increase computational burden and implementation complexity. Other approaches include topological modifications, such as alternative switch arrangements, the incorporation of reactive components [19], variable transformers [20], and variable switching frequency techniques [21].

In contrast, the use of a magnetically controlled Variable Inductor (VI), first introduced in a Dual-Active-Half-Bridge (DAHB) converter for solid-state transformer (SST) applications [22], and later extended to full-bridge DAB converters [23], provides an additional physical degree of freedom. A VI is an electromagnetic device whose inductance can be dynamically adjusted by injecting a small DC current (i_{bias}) into auxiliary windings in the magnetic core.

The i_{bias} shifts the magnetic operating point along the nonlinear region of the B–H curve, enabling dynamic adjustment of the power transfer inductance (L_{DAB}) as a function of i_{bias}. This allows the extension of the ZVS range under light-load conditions and the reduction of circulating reactive power at high load. As a result, the transfer inductance can be continuously adapted to the operating conditions without increasing system complexity. In this context, the proposed approach preserves the simplicity of the mathematical analysis associated with conventional PS modulation. Moreover, from a control perspective, PI controllers can be used to control the inductance, which are widely recognized for their simplicity, robustness, and ease of implementation, as demonstrated in previous works [23], [22]

Beyond efficiency improvements, the ability to modify the transfer inductance enables a partial linearization of the converter transfer function, facilitating control design and enhancing dynamic performance [23]. In addition, inductance modulation can extend the maximum power transfer capability as the PS approaches its operational limits [23]. Since the inductance directly affects the converter plant, the authors in [23] propose an inductance compensation loop operating in conjunction with the PS. Their results demonstrate a significant improvement in dynamic response when comparing load-step transients using only PS control versus the combined PS and VI approach. Furthermore, the use of a VI mitigates the fundamental design trade-off associated with L_{DAB} in conventional DAB converters, as discussed in [24].

However, the existing literature lacks studies addressing the application of VI in DAB converters for battery charging, particularly for efficiency optimization through the combined adjustment of PS and inductance. Previous works [22], [23] mainly focus on SST applications and evaluate the efficiency influence of a single control parameter, which limits the identification of globally optimal operating conditions. In contrast, this work proposes a dual-parameter experimental optimization strategy based on a combined sweep of L_{DAB} and PS for each operating point along the battery charging trajectory.

Unlike applications with a static DC bus, battery charging imposes a specific load trajectory defined by the Constant Current–Constant Voltage (CC–CV) profile, in which the output voltage (V_{out}) and output power (P_o) vary simultaneously during the charging process.

For a fair performance assessment, the proposed approach is compared with a conventional DAB employing a fixed inductance (FI-DAB), ensuring that efficiency gains are not biased by intrinsic losses associated with VI structures.

Finally, the effectiveness of the proposed approach is evaluated using the Time-Weighted Overall Efficiency (η_{total}), which accounts for the entire charging cycle of the BESS. This figure of merit allows the performance improvement to be quantified in a practical scenario, extending the analysis beyond isolated operating points.

A preliminary version of this work was presented in [25]. This paper extends and revises that work by providing additional technical contributions. The main extensions are summarized as follows: (i) restriction of the application scope to battery energy storage systems (BESS); (ii) a detailed design methodology for the VI, including a nonlinear magnetic model to guide its design; (iii) improved inductance measurement accuracy through the inclusion of additional measurements based on the first-harmonic approach, as discussed in [26]; (iv) a time-weighted efficiency analysis over the complete charging cycle; and (v) additional experimental results and analyses, particularly under light-load conditions.

The remaining paper is organized as follows. Section II presents the principles of operation of the converter and the main equations of DAB converter. Section III introduces the VI and the magnetic circuit analysis. Section IV discusses the design of the converter, including the FI and VI, the variation of PS, as well as the tests conducted in the BESS to determine the converter load range. Section V outlines the experimental setup and the methodology for extracting the optimized points of the PS and L_{DAB} employing the prototype developed in the laboratory. Section VI presents the conclusions of the work.

II. DAB CONVERTER TOPOLOGY

The DAB converter topology comprises two full-bridge converters interconnected by an inductor (L_{DAB}) and a high-frequency transformer, Fig. 1.

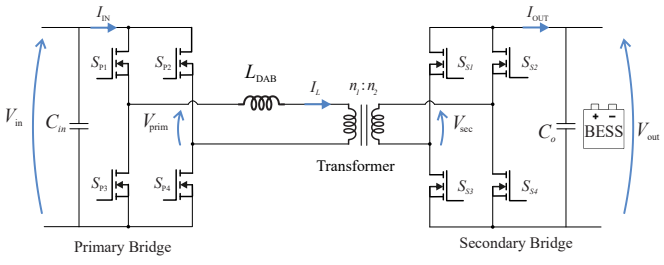

FIGURE 1. DAB converter with a fixed inductor realizes the interface between the DC BUS and the BESS.

In SPS modulation, the power flow is controlled by the PS (ϕ) between the voltages of two full-bridge converters. The power flow of SPS is expressed as

$$P_o = \frac{V_{\text{in}} V_{\text{out}} \phi}{2\pi f_s L_{\text{tot}} n \left(1 - \frac{|\phi|}{\pi}\right)}, \tag{1}$$

where V_{in} is the input DC bus voltage, V_{out} is the output voltage (BESS voltage), L_{tot} is the total inductance, which is the sum of the auxiliary inductance L_{DAB} and the transformer's leakage inductance, n is the transformer turns ratio, respectively. f_s is the switching frequency. Equation 1 clarifies the L_{tot} and ϕ dependence for power transfer.

A. ZVS boundaries

The voltage conversion ratio (d) plays a crucial role in the performance of the DAB converter, as it directly affects the ZVS boundaries and the circulating currents. This ratio is expressed as

$$d = \frac{nV_{out}}{V_{in}}. \tag{2}$$

From (2), it can be observed that d depends on both V_{in} and V_{out}. In this study, V_{in} is considered constant, while V_{out} varies during the BESS charging and discharging processes. Achieving a ($d = 1$) is desirable from the perspective of ZVS and also for reducing the circulating reactive energy in the converter [24]. However, maintaining $d = 1$ is challenging in BESS applications.

The parameter n directly influences the ZVS boundaries. Therefore, several studies in the literature have addressed the optimization of this design parameter [6], [24], [27]. In this work, n was selected as 8:1, considering the nominal voltage of the BESS (24 V). Under these nominal conditions, the design aims to achieve $d \approx 1$.

In practical implementations, however, non-idealities, such parasitic capacitances, leakage and magnetizing inductances, and dead-time effects—further impact the ZVS regions. Recent research has therefore proposed refined modeling approaches to accurately define these boundaries in BESS applications [5], [6]. Based on the established design, the ZVS analysis is conducted using (3) and (4) expressions, which offer a more straightforward representation of ZVS boundaries. Additionally, from a general perspective, these boundaries depend on the BESS load profile, which vary for different battery technologies and charging conditions.

In addition to the d, achieving ZVS in the converter switches requires that the inductor current be sufficient to discharge the intrinsic capacitances of the switches during the commutation intervals.

By analyzing the converter operating stages and the inductor current behavior, equations can be derived to establish the PS required for ZVS in both primary (ϕ_x) and secondary (ϕ_y) switches. The ZVS boundaries can be expressed as

$$\phi_x(d) = \frac{\pi(d-1)}{2d} \tag{3}$$

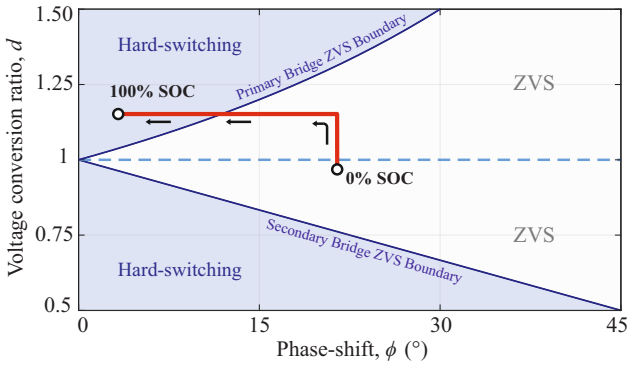

FIGURE 2. With a fixed inductor, the BESS load profile (in red) crosses the ZVS boundaries and the converter loses ZVS near the end of charge.

$$\phi_y(d) = \frac{\pi(1-d)}{2} \tag{4}$$

The ZVS boundaries of the DAB converter are illustrated in Fig. 2. The red line represents the simulation results of the DAB operating along the battery charging trajectory using a FI with $L_{\text{tot}} = 42.8$ μH under PS modulation. This inductance value, along with all other simulated parameters, corresponds to those used in the experimental setup, including the leakage inductance of the high-frequency transformer. It can be observed that, under ideal conditions with a unity voltage conversion ratio ($d = 1$), the converter achieves ZVS over the entire PS range (ϕ). However, increasing ϕ leads to higher circulating reactive power within the converter.

By analyzing Fig. 2, it can be observed that as the BESS approaches a state of charge (SOC) close to 100%, the converter reaches hard-switching conditions for the primary-side switches. This is a critical condition, since the primary side operates at the high-voltage level. By employing the VI, it becomes possible to adjust the ϕ trajectory so that it remains within the ZVS boundaries at low load conditions, while allowing operation with low PS at higher loads, thereby reducing the circulating reactive energy in the converter.

III. DAB DESIGN

This section presents the operating principle and design methodology of the VI, including the magnetic circuit analysis and the extraction of the battery load profile. The design of the conventional FI is first introduced, followed by the proposed VI. The VI performs the same role as the FI while using the same core size, but enables inductance variation through controlled core saturation, allowing improved operation over a wide load range.

A. VI Principle of Operation and Magnetic Circuit Analysis

Different implementation structures for variable inductors are explored in the literature, including the triple-E structure [28], the quadruple-E structure [29], and toroidal core structures [30]. In this work, the double-E configuration is

adopted, as it is the most widely used and well-understood topology in the literature [31]–[33].

In this core structure, the main windings are placed on the central magnetic leg, with the number of turns denoted by N_{ac}. The auxiliary control windings are located on the external legs and have a number of turns denoted by N_{dc}. These control windings are connected in series with opposite polarity in order to cancel out the AC voltages induced by the central leg.

By injecting a DC bias current i_{bias} into the auxiliary windings, a unidirectional magnetic flux is established that links the main winding. This DC flux shifts the magnetic operating point of the core into its nonlinear region, thereby modifying the effective permeability of the magnetic material and, consequently, varying the inductance observed in the main winding [34].

The design of double-E core variable inductors is extensively discussed in [32] [34], [33] [35]. Fig. 3(b) illustrates the equivalent magnetic circuit of the variable inductor, as proposed by the authors in [34]. In this model, R_{gap} represents the constant reluctance of the air gap, while R_c, R_l, and R_r denote the reluctances of the central, left, and right magnetic paths, respectively. These are functions of the magnetic permeability (μ) of the core material. Unlike conventional magnetic materials, where the permeability may vary only under high current or temperature levels that drive the core into saturation, in variable magnetic devices, the permeability changes continuously according to the operating point along the *B–H* curve. This behavior is a direct consequence of the i_{bias} applied to the auxiliary windings. The voltage sources in the equivalent circuit represent the magnetomotive forces generated by the auxiliary windings ($N_b \cdot I_b$ and $N_b \cdot I_b$), as well as by the main winding ($N_{ac} \cdot I_{ac}$).

The inductance of the main winding can be expressed as

$$L_{\text{var}} = \frac{N_{\text{ac}}^2}{R_c + R_g + \frac{R_l R_r}{R_l + R_r}}. \tag{5}$$

Each reluctance path R_x depends on the differential permeability and can be modeled as

$$R_x = \frac{l_x}{\mu_{\text{diff}}(H_x)\,\mu_0 A_x} \tag{6}$$

The number of turns in the auxiliary windings can be defined as

$$N_c = \frac{H(\mu_{\text{diff}})\,l_{\text{ext}}}{I_{\text{bias}}} \tag{7}$$

where μ_{diff} is the material's permeability behavior as a function of magnetic field intensity H_x, l_{ext} is the external magnetic path length, and A_x is the core's path cross-sectional area.

B. Characterization of the BESS Charging Load Profile

To characterize the load range processed by the DAB converter during battery charging, an experimental procedure was conducted using an industrial cyclic battery tester

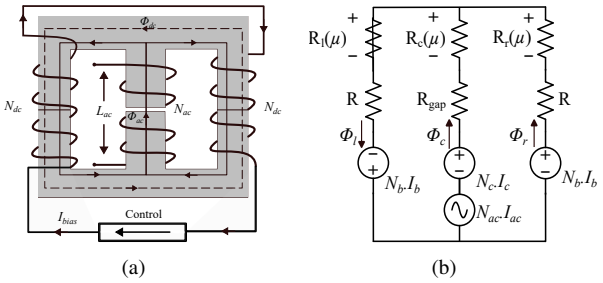

FIGURE 3. Variable inductor based on double E-core structure. (a). Equivalent Reluctance circuit (b).

(model IDCLT 100A30V) manufactured by iDevices. The procedure followed the battery manufacturer's recommended charging method, which adopts the CC–CV profile.

The BESS consists of 12 lead-acid cells, each rated at 2 V and 250 Ah (EnerSys®), connected in series to form a 24 V bus. The charging process was carried out under a constant current of 21 A until V_{out} reached 28.8 V, marking the transition to the CV stage. In this stage, the charging current naturally decreases, and the charging process is completed when the current reaches the end-of-charge threshold, as depicted in Fig. 4.

It is also important to emphasize that, upon completion of the charging process, lead-acid batteries are maintained under float charging conditions for extended periods in order to compensate the self-discharge. Under these conditions, the use of a FI-DAB leads to operation with low PS values. Low PS reduces the energy available for resonant transitions, which compromises the achievement of ZVS in the converter. Furthermore, operation at very low PS values degrades controllability, as the dead-time becomes significant relative to the PS. This aspect is further discussed in the experimental validation section.

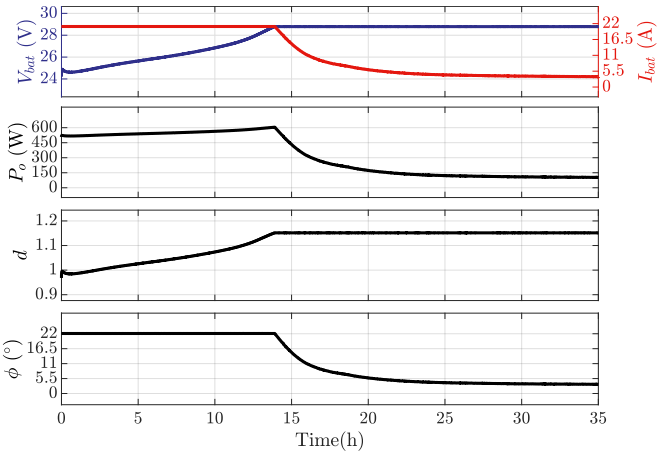

FIGURE 4. Experimental battery load profile.

C. FI design

Based on the extracted BESS load profile, the power range from 100 W to 600 W defines the design constraints for the FI-DAB as the energy transfer element. The FI is designed considering the maximum power transfer condition of 600 W. To determine the required inductance, a nominal phase shift ϕ_n is fixed as a design parameter, and L_{tot} is obtained from (1) defining a $\phi = \phi_n$, with $\phi_n = 27°$.

The selection of ϕ_n in the range of 20°–30° is commonly adopted in the literature as a design guideline to reduce circulating reactive energy under high-load conditions [24], [27]. In this context, ϕ_n must be fixed to enable the determination of the inductance. Lower values of ϕ_n are preferable to ensure efficient operation at 600 W, as they reduce the circulating current.

Conversely, increasing ϕ_n leads to a higher L_{tot}. While this benefits light-load operation by enabling larger PS values, thereby expanding the ZVS boundaries and improving efficiency, it becomes detrimental at high power levels. In such cases, the required PS becomes large, increasing the circulation of reactive energy.

The design parameters of FI are detailed in Table 1, resulting in a L_{tot} of 42.8 μH with L_{DABF} at 35 μH. Employing an $AeAw$ methodology, the physical inductor is made of double E ferrite core (E30/14/15, IP12R material). The inductor was designed using the $A_e A_w$ methodology and implemented with a double E ferrite core (E30/14/15, IP12R material). Inductance measurement was carried out using a high-precision LCR meter Keysight E4980A 20 Hz - 1 MHz. Fig. 6 illustrates the FI in the DAB converter prototipe.

TABLE 1. Design parameters of the DAB converter.

Parameter	Value	Symbol
Input Voltage	200 V	V_{in}
Output Voltage	23 V – 28.8 V	V_{out}
Nominal Output Power	600 W	P_{o}
Switching Frequency	100 kHz	F_{s}
Transformation Ratio	1:8	n
Output Capacitance	200 μF	C_{o}
Transformer Leakage Inductance	7.8 μH	L_{lk}
Core Type (FI and VI)	E ferrite core (E30/14/15, IP12R material)	–
FI Inductance	35 μH	L_{DABF}
FI Turns	7	N_{FI}
VI Range	15 – 300 μH	L_{DABV}
VI Turns	16	N_{VI}
VI Auxiliary Winding Turns	30	N_{aux}
FI DC Resistance	55.18 mΩ	$R_{\text{dc,FI}}$
FI AC Resistance	102.56 mΩ	$R_{\text{ac,FI}}$
VI DC Resistance	61.57 mΩ	$R_{\text{dc,VI}}$
VI AC Resistance	863.71 mΩ	$R_{\text{ac,VI}}$

D. VI design

The maximum inductance of the VI, L_{max}, is defined based on the minimum output power condition ($P_o = 100$ W) at $V_{\text{out}} = 28.8$ V. Under these conditions, a relatively large PS is required to provide sufficient reactive energy to ensure ZVS. For $P_o = 100$ W, a PS of $\phi = 27°$ guarantees ZVS for the primary switches, according to (3). By substituting $\phi = 27°$ and the parameters from Table 1 into (1), the maximum inductance is obtained as $L_{\text{max}} = 300$ μH at $i_{\text{bias}} = 0$.

Conversely, to achieve maximum output power while reducing circulating reactive energy, a lower PS is required, which in turn requires a smaller inductance value. Therefore, the minimum inductance (L_{min}) is defined at the maximum excursion of the B–H curve, corresponding to the peak control current of $i_{\text{bias}} = 1.5$ A. Under this condition and applying (5), the VI inductance is reduced to 15 μH. When considering the additional contribution of the transformer leakage inductance (L_{lk}), the total effective series inductance becomes 22.8 μH. This results in a theoretical $\phi = 14°$, which minimizes circulating reactive energy while maintaining feasible operating conditions for the converter.

With the inductance range, the magnetic design is carried out. The number of turns of the auxiliary winding (N_c) is determined from (7) considering the maximum control current ($i_{\text{bias}} = 1.5$ A). The number of turns in the main winding is obtained from (5), resulting in $N_{ac} = 16$ turns.

The VI is implemented using the same core size and magnetic material as the FI to ensure a fair efficiency comparison. The inductor is constructed using Litz wire (AWG 30) with 23 parallel strands.

Finally, the inductance profile is experimentally characterized using a Keysight E4980A LCR meter (20 Hz - 1 MHz) Fig. 7 (a) shows the measured inductance as a function of i_{bias}.

IV. EXPERIMENTAL RESULTS

The experimental setup, illustrated in Fig. 5, comprises a programmable DC electronic load (Keysight 2380-500-30) configured in constant voltage mode to emulate the BESS voltage. The efficiency measurements were performed using a high-accuracy power analyzer (Yokogawa WT1800E). The input DAB converter DC bus is sourced by a Keysight 6812B DC power supply, while an auxiliary DC source provides the i_{bias} and energizes the motherboard circuitry. Signal acquisition and FFT analysis for inductance characterization were conducted using a Tektronix MSO 46 oscilloscope.

A DAB converter prototype was developed based on the parameters specified in Table 1, as shown in Fig. 6. The power stage consists of two full-bridge modules implemented on independent Printed Circuit Boards (PCBs). The primary bridge utilizes IPP220N25NF MOSFETs, whereas the secondary side employs IPB042N10N3F devices. Both stages are interconnected through a high-frequency transformer and the inductance (VI or FI). The switch control stage is implemented via a Texas Instruments F28379D C2000 Digital Signal Processor (DSP), interfacing with the power stage through eight VO3120 gate drivers.

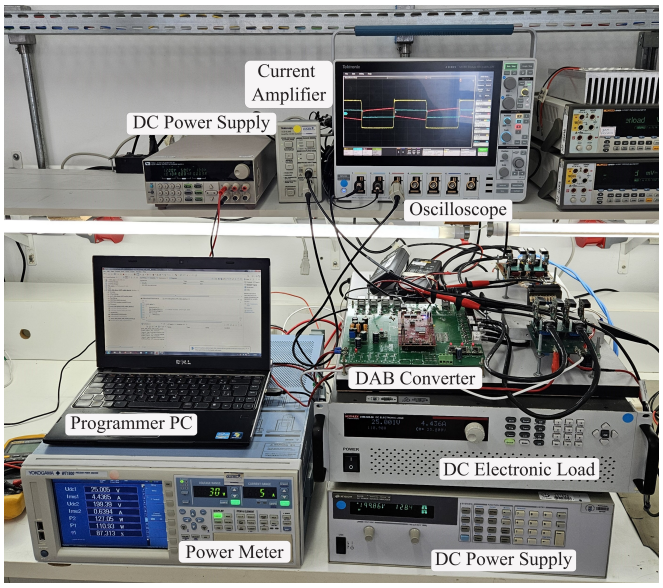

FIGURE 5. Experimental SETUP.

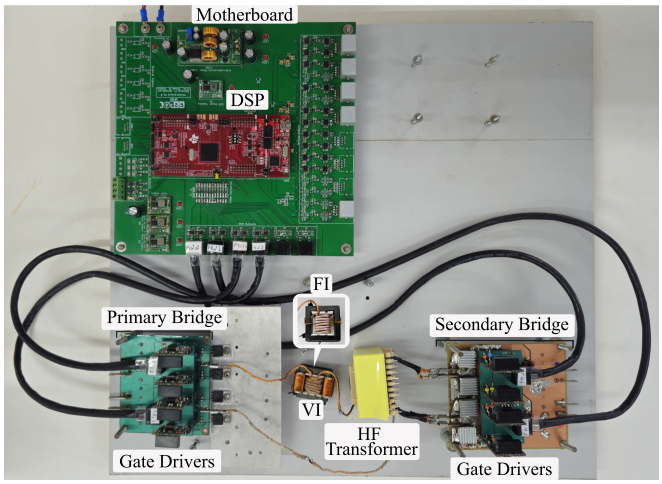

FIGURE 6. DAB converter experimental prototype.

A. Inductance Characterization Based on Fundamental Harmonic

In order to improve the accuracy when tracing the inductance curve L_{DABV} as a function of i_{bias}, a simplification based on the RMS value of the fundamental harmonic component of the measured inductor voltage and current is applied, as described in [26]. The impedance calculation is given by

$$L_{\text{DABV}} = \frac{X_L}{\omega} = \frac{V_L}{I_L} \cdot \frac{\pi/4}{2\pi f_s}, \tag{8}$$

since the RMS amplitude of the fundamental harmonic component of the voltage and current waveforms is measured, (8) can be rewritten as

$$L_{\text{DABV}} = \frac{X_L}{\omega} = \frac{V_{\text{rms}}}{I_{\text{rms}}} \cdot \frac{1}{2\pi f_s} \tag{9}$$

where V_L denotes the RMS amplitude of the fundamental harmonic component of the inductor voltage, and I_L refers to the RMS amplitude of the corresponding current component.

Fig. 7 (a) shows, in blue, gray, and orange, the measurements obtained for three different output voltages. The data were obtained through harmonic analysis. By analyzing the figure, it can be observed that the variation among the curves for different output voltages is relatively small. However, a noticeable difference can be observed when comparing these results with the inductance values measured using the LCR meter, particularly for i_{bias} values close to zero.

This difference occurs due the LCR meter performs the measurement by injecting small sinusoidal signals, whereas in practical operation the DAB converter produces square-wave voltages containing significant harmonic components.

Finally, the waveform measurements used for the calculations are illustrated in Fig. 8 (a), corresponding to $i_{bias} = 0$ A, and in Fig. 8 (b), corresponding to $i_{bias} = 1$ A).

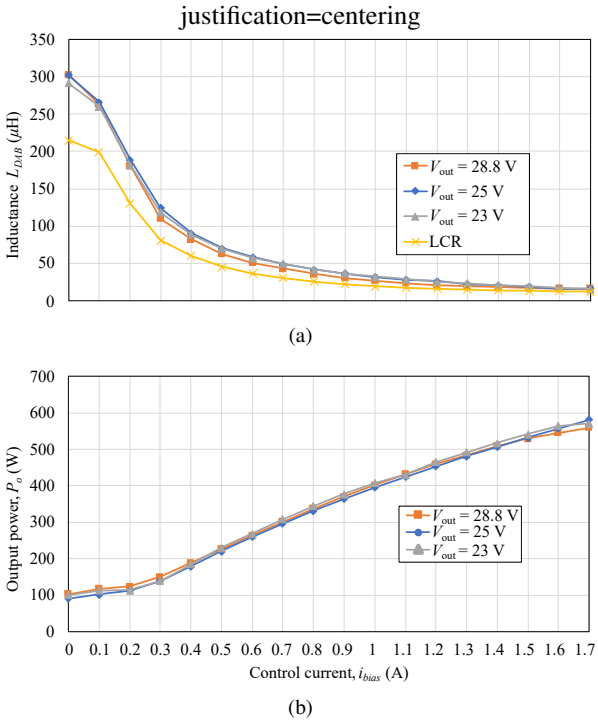

FIGURE 7. Inductance L_{DABV} as a function of i_{bias} (a). Effect of inductance variation on power transfer of DAB converter (b).

B. Impact of inductance variation on power transfer

The reduction in inductance leads to an increase in the output power of the DAB converter. To illustrate this behavior, Fig. 7 (a) presents the inductance curve L_{DABV} as a function of i_{bias}, while Fig. 7 (b) shows the P_o versus i_{bias} for $\phi = 35°$.

C. Experimental methodology for tracking efficiency points of FI-DAB

The experimental efficiency results of the FI-DAB were obtained by sweeping P_o from 15 W to 600 W, across three different output voltages: 23 V ($d = 0.85$), 25 V ($d = 1$), and 28.8 V ($d = 1.15$), using only PS as the

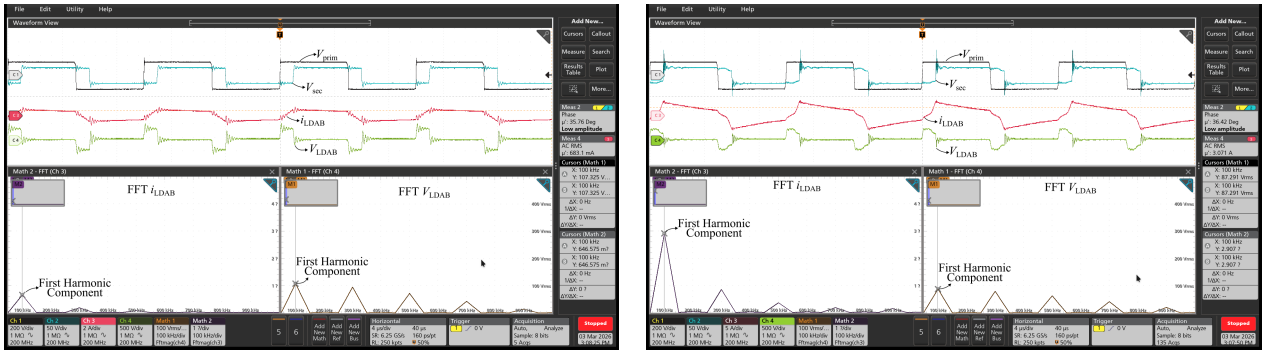

(a) (b)

FIGURE 8. Experimental waveforms for first harmonic approximation: (a) CH1 - V_{prim}; CH2 - V_{sec}; CH3 - $i_{L_{DAB}}$; CH4 - V_{LDAB}. i_{bias} = 0; (b) i_{bias} = 1 A.

control variable. Fig. 9 (b) illustrates the efficiency map of the FI-DAB, where measured data is represented by white points. The efficiency heatmap was generated by applying a cubic fitting tool to interpolate experimental data, providing a comprehensive overview of the converter's performance across a wide operational range. This analysis quantifies the impact of load variations and voltage fluctuations on the efficiency of a traditional converter with fixed inductance. Consequently, it establishes a baseline to evaluate the efficiency enhancement achieved by the VI at equivalent operating points. Furthermore, the battery charging profile introduced in Fig. 4 is superimposed on the efficiency map in Fig. 9 to provide a clearer graphical representation of the d and P_o trajectory during a typical charging cycle.

D. Experimental method for tracking optimized efficiency points of VI-DAB

In the VI-DAB configuration, various combinations of L_{DABV} and ϕ can satisfy a specific P_o. To identify the optimal L_{DABV} and ϕ pairs that achieve the target P_o and d with maximum efficiency, a manual sweep of i_{bias} was performed in 0.1 A increments. During this process, ϕ was adjusted to maintain the desired P_o, while d was kept constant by the electronic DC load. Consequently, the efficiency was measured across these operating points to identify the peak efficiency.

In the proposed methodology, the i_{bias} is swept across a variable range determined by the load conditions. For high-power levels, a decreasing i_{bias} sweep is applied, whereas an increasing sweep is used for low-power levels. The sweep range is constrained by practical operating limits: at high loads, the sweep terminates when efficiency decreases at $\phi > 30°$; at low loads, the process is interrupted as the ϕ approaches $5°$ to ensure a feasible modulation range. These optimal operating points are indicated by the white markers in Fig. 9 (a).

This experimental characterization was conducted using the same P_o and d values as the FI-DAB analysis. The remaining regions of the efficiency map were interpolated using the same cubic method employed for the FI-DAB.

E. Efficiency Comparative Analysis: Case Study Discussion

To characterize the optimal combinations of L_{DABV} and ϕ, and to evaluate the high-efficiency operating points experimentally obtained with the VI, three representative case studies were analyzed. These cases correspond to key operating conditions along the battery charging profile and are highlighted with the corresponding numbers in Fig. 9.

The analyzed cases are defined as follows:

- Case 1 (Initial Charging Stage):$P_o = 500$ W and $V_{out} = 25$ V ($d = 1$), representing the initial high-power charging stage.
- Case 2 (Maximum Power Stress): $P_o = 600$ W and $V_{out} = 28.8$ V ($d = 1.15$), identifying the converter's performance at its upper power and voltage limits.
- Case 3 (End-of-Charge / ZVS loss): $P_o = 100$ W and $V_{out} = 28.8$ V ($d = 1.15$), a light-load condition where traditional FI-DAB loses ZVS.

In addition, for direct comparison, Fig. 10 presents the efficiency difference $\Delta\eta$ between the VI-DAB and FI-DAB. Positive values of $\Delta\eta$ indicate efficiency gains with the VI-DAB, whereas negative values represent efficiency degradation compared to the FI-DAB. This figure will be further discussed in conjunction with the selected case studies.

1) Case 1

At experimental point 1, the converter operates at $P_o = 500$ W and $V_{\text{out}} = 25$ V ($d = 1$). In the Fig 10, an efficiency gain of 2.18% is observed. This is primarily due to a significant reduction in the PS from 33.9° (FI) to 15.6° (VI), representing an 18.3 % reduction. In this case, the use of the VI enables reduced reactive power circulation by decreasing ϕ. The inductance also decreases from 35 μH (FI) to 18.56 μH (VI), contributing to reduced conduction losses. Table 2 summarizes the sweep results for Case Study 1, highlighting the operating points associated with maximum efficiency. It is observed that the highest efficiency (highlighted in bold) does not necessarily coincide with

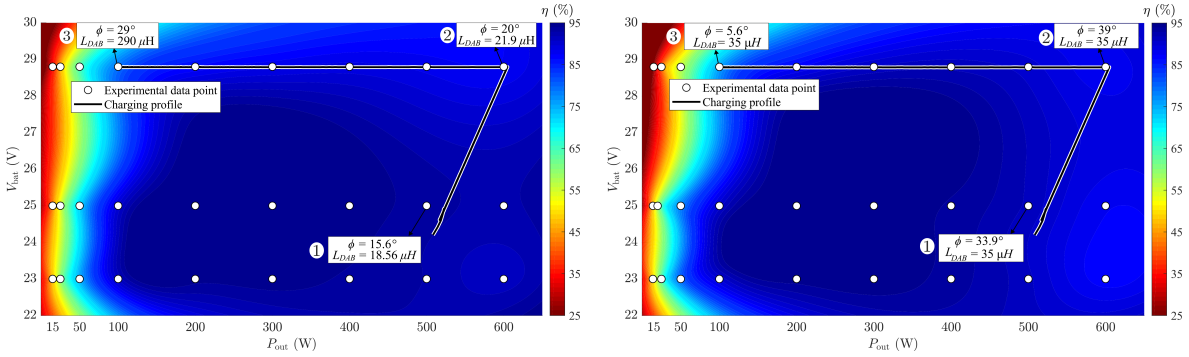

FIGURE 9. Efficiency maps. (a) VI (considering control winding losses); (b) FI.

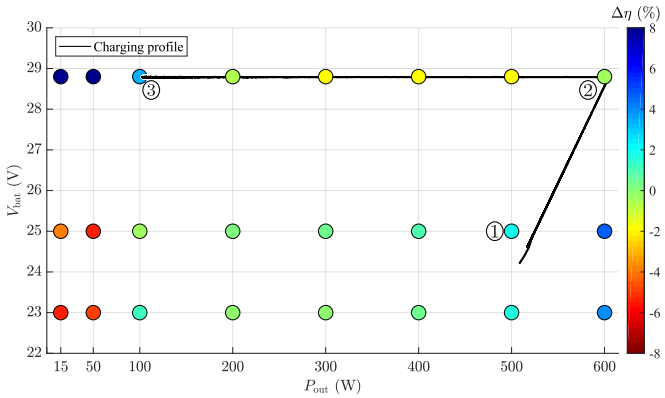

FIGURE 10. Efficiency difference $\eta_{\text{VI-DAB}}$ - $\eta_{\text{FI-DAB}}$ ($\Delta\eta$).

TABLE 2. Sweep results for Case Study 1: $P_o = 500$ W and $V_{\text{out}} = 25$ V ($d = 1$). The highest efficiency point is highlighted in bold.

L_{DAB} (µH)	i_{bias} (A)	ϕ (°)	η (%)	P_{in} (W)
VI-DAB Sweep				
18.57	1.5	15.6	93.394	535.37
20.49	1.4	15.9	93.260	536.14
21.92	1.3	16.1	93.185	536.57
28.18	**1.1**	**19.7**	**93.537**	**534.55**
36.46	0.9	27.3	92.219	542.19
41.48	0.8	63.0	86.885	575.47
FI-DAB				
35.00	–	33.9	91.36	547.01

the minimum inductance value, since the increased i_{bias} effort under certain conditions does not offset the additional losses in the auxiliary winding. Furthermore, the maximum efficiency is achieved at an operating point close to the magnetic saturation region.

2) Case Study 2

At experimental point 2, the converter operates at $P_o = 600$ W and $V_{\text{out}} = 28.8$ V. In the Fig. 10 a not efficiency enhancement is observed, despite the lower ϕ employed. This outcome suggests that the optimal operating point may lie between the discrete i_{bias} steps considered in the sweep, or that increased core, and winding losses of VI counterbalance the reduction in circulating currents.

Table 3 presents the sweep results for Case Study 2, highlighting that the points of highest efficiency also occur near the maximum saturation region.

TABLE 3. Sweep results for Case Study 2: $P_o = 600$ W and $V_{\text{out}} = 28.8$ V ($d = 1.15$). The highest efficiency point is highlighted in bold.

L_{DAB} (µH)	i_{bias} (A)	ϕ (°)	η (%)	P_{in} (W)
VI-DAB Sweep				
16.73	1.5	19.4	88.027	681.61
17.71	1.4	19.7	88.075	681.24
19.34	**1.3**	**20.0**	**88.154**	**680.62**
20.68	1.2	23.3	87.963	682.11
23.45	1.1	25.0	87.398	686.52
26.61	1.0	30.0	85.835	699.01
FI-DAB				
35.00	–	39.0	88.42	678.8

3) Case Study 3

At experimental point 3, the converter operates at 100 W and $V_{\text{out}} = 28.8$ V ($d = 1.15$). In this condition, the FI-DAB converter fails to achieve ZVS. This occurs because the $\phi = 5.6°$ is insufficient to provide the necessary reactive energy to discharge the MOSFET output capacitances. In contrast, at point 3, a sweep resulted in an efficiency improvement of 3.34 %, enabled by a higher PS of $\phi = 29°$.

Table 4 presents the sweep results for the case study. At this operating point, an intermediate step ($i_{\text{bias}} = 0.05$ A) was employed to explicitly capture the maximum efficiency between discrete points. It is also noted that a high ϕ under these conditions restores ZVS operation.

Fig. 10 shows that, for power levels below 100 W at $V_{\text{out}} = 28.8$ V ($d = 1.15$), significant efficiency gains of approximately 8% are achieved. These improvements, enabled by the VI, occur mainly under operating conditions

TABLE 4. Sweep results for Case Study 3: $P_o = 100$ W and $V_{out} = 28.8$ V ($d = 1.15$). The highest efficiency point is highlighted in bold.

L_{DAB} (µH)	i_{bias} (A)	ϕ (°)	η (%)	P_{in} (W)
VI-DAB Sweep				
92.39	0.4	6.5	75.570	132.11
120.44	0.3	8.5	76.612	130.39
191.44	0.2	17.0	78.715	126.98
273.54	0.1	25.7	78.980	126.59
290.60	**0.05**	**30.0**	**79.350**	**125.96**
313.71	0.0	40.0	78.300	127.71
FI-DAB				
35.00	–	5.6	76.000	131.6

in which the FI-DAB converter loses ZVS. As illustrated in Fig. 11, the use of the VI significantly improves the thermal performance of the primary-side switches. When using the FI (Fig. 11 (a)), the ZVS condition is lost, causing the switches to reach approximately 72.3 °C despite the relatively large heatsink in the prototype. In contrast, the VI maintains ZVS (Fig. 11 (b)), lowering the maximum switch temperature to 56.4 °C. These measurements were obtained under thermal equilibrium conditions using a Fluke Ti25 thermal imaging camera. In contrast, for output voltages of 25 V ($d = 1$) and 23 V ($d = 0.85$) under light-load conditions (below 100 W), a reduction in efficiency is observed with the VI, even when employing a maximum-efficiency search strategy. However, under nominal load conditions (600 W) at $V_{out} = 25$ V, the use of the VI results in significant efficiency improvements.

Additionally, operation of the FI-DAB at low power levels requires reduced ϕ, which degrades control linearity. Under these conditions, the system becomes highly sensitive to dead-time effects, a phenomenon widely referred to in the literature as phase-drift. This sensitivity limits the effective phase resolution, making stable converter operation more challenging. This limitation is evidenced in Fig. 9 (b), where operation at 25 W using the FI-DAB was not achievable due to phase resolution constraints; consequently, the efficiency difference at this operating point was not computed in Fig. 10. For instance, at $P_o = 15$ W and $V_{out} = 25$ V, the FI-DAB operates with a very small PS of $\phi = 1.39°$. In contrast, the VI-DAB achieves an optimal operating point with $\phi \approx 8°$ and $i_{bias} = 0$, highlighting its ability to maintain improved controllability under the same power conditions.

In this context, the VI presents a key advantage: even at operating points where efficiency is slightly lower, the use of variable inductance enables operation with significantly higher ϕ values for the same output power. This reduces the system sensitivity to disturbances and substantially improves control robustness and stability under light-load conditions.

The reduced efficiency observed in the VI-DAB converter is primarily attributed to increased ohmic losses, stemming from its structure with a higher number of windings. As shown in Table 1, the AC resistance is significantly, from 102.56 mΩ (FI) to 863 mΩ (VI). Additional losses are associated with additional energy in the auxiliary windings and potential increases in core losses. This behavior is also observed at $V_{out} = 28.8$ V for P_o values of 300 W, 400 W, and 500 W. Efficiency can be improved by optimizing the VI design to reduce inductance excursion and winding resistance. This also contributes to reduction of L_{DABV} near core saturation, leading to smaller ϕ under high-load conditions. During battery charging, however, the converter typically operates for limited periods within these regions; therefore, the corresponding operating time will be considered in the next subsection.

F. Time-Weighted Overall Efficiency

To more accurately quantify the efficiency gains throughout the battery charging process, the ideal approach would involve continuous measurements of the converter's efficiency over the entire charging cycle. Based on such measurements, the system's overall energy efficiency could be determined by calculating the ratio between the total energy delivered to the load and the total energy drawn from the source.

Nevertheless, implementing this procedure in practice is time-consuming, as the complete charging process of the batteries is inherently slow. Due to this limitation, an alternative methodology was adopted, based on regression fitting of the experimental efficiency data obtained from the converter's efficiency maps. Using this fitted data, the time-weighted overall efficiency was estimated, as described in (10):

$$\eta_{total} = \frac{\int_0^T P_{out}(t), dt}{\int_0^T P_{in}(t), dt} \tag{10}$$

The total efficiency of the approaches is shown in Table 5.

TABLE 5. Comparison of time-weighted total efficiencies.

Approach	Efficiency (%)	Difference (%)
Fixed Inductance	88.09	—
Variable Inductance	89.53	1.44

V. CONCLUSION

This article presented an approach to optimize the efficiency of a DAB converter using a VI for BESS applications.

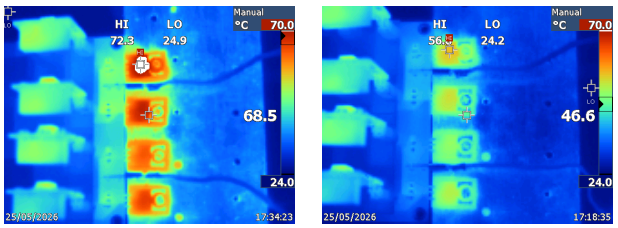

(a) (b)

FIGURE 11. Infrared thermal image of the primary-side switches for the operating point: $V_{out} = 28.8$ V, $P_o = 50$ W, and $d = 1.15$. (a) using FI where ZVS is lost; and (b) using VI.

A manual sweep was proposed to determine the optimal operating conditions for maximum efficiency across different power and voltage levels. The experimental results demonstrated that optimizing the operating points via inductance variation reduces both conduction and switching losses, thereby improving converter efficiency, particularly under extreme load conditions. Specifically, the VI-DAB achieved a peak efficiency gain of 8% under light-load conditions and 2.18% under high-load conditions compared to the FI-DAB. Furthermore, when evaluating a complete charging cycle using time-weighted efficiency, the VI-DAB approach yielded an overall efficiency gain of 1.44%. Furthermore, the VI-DAB improved PS resolution at light loads, ensuring more robust and linear control compared to the FI-DAB. For future work, the design of a VI with a small range of excursion is suggested, aiming to optimize efficiency in operating regions where the VI-DAB did not outperform the FI-DAB.

AUTHOR'S CONTRIBUTIONS

C.G.MARQUES: Conceptualization, Formal Analysis, Investigation, Methodology, Project Administration, Resources, Software, Validation, Visualization, Writing – Original Draft, Writing – Review & Editing. **J.P.S.CIPRIANI:** Conceptualization, Data Curation, Formal Analysis, Investigation, Methodology, Writing – Original Draft, Writing – Review & Editing. **L.ROGGIA:** Formal Analysis, Investigation, Methodology, Project Administration, Validation, Writing – Original Draft, Writing – Review & Editing. **M.S.PERDIGÃO:** Conceptualization, Formal Analysis, Methodology, Project Administration, Writing – Original Draft, Writing – Review & Editing. **J.R.TIBOLA:** Conceptualization, Data Curation, Formal Analysis, Investigation, Methodology, Validation, Writing – Original Draft, Writing – Review & Editing. **A.R.SEIDEL:** Conceptualization, Formal Analysis, Funding Acquisition, Investigation, Methodology, Project Administration, Resources, Supervision, Writing – Original Draft, Writing – Review & Editing.

PLAGIARISM POLICY

This article was submitted to the similarity system provided by Crossref and powered by iThenticate – Similarity Check.

DATA AVAILABILITY

The data used in this research is available in the body of the document.

REFERENCES

[1] M. Kheraluwala, R. Gascoigne, D. Divan, E. Baumann, "Performance characterization of a high-power dual active bridge DC-to-DC converter", *IEEE Transactions on Industry Applications*, vol. 28, no. 6, pp. 1294–1301, 1992, doi:10.1109/28.175280.

[2] D.-K. Jeong, H.-S. Kim, J.-W. Baek, J.-Y. Kim, H.-J. Kim, "Dual active bridge converter for Energy Storage System in DC microgrid", *in 2016 IEEE Transportation Electrification Conference and Expo, Asia-Pacific (ITEC Asia-Pacific)*, pp. 152–156, 2016, doi:10.1109/ITEC-AP.2016.7512939.

[3] R. Morrison, M. Egan, "A new power-factor-corrected single-transformer UPS design", *IEEE Transactions on Industry Applications*, vol. 36, no. 1, pp. 171–179, 2000, doi:10.1109/28.821812.

[4] L. Chen, F. Gao, K. Shen, Z. Wang, L. Tarisciotti, P. Wheeler, T. Dragičević, "Predictive Control Based DC Microgrid Stabilization With the Dual Active Bridge Converter", *IEEE Transactions on Industrial Electronics*, vol. 67, no. 10, pp. 8944–8956, 2020, doi:10.1109/TIE.2020.2965460.

[5] O. Zayed, A. Elezab, A. Abuelnaga, M. Narimani, "A Dual-Active Bridge Converter With a Wide Output Voltage Range (200–1000 V) for Ultrafast DC-Connected EV Charging Stations", *IEEE Transactions on Transportation Electrification*, vol. 9, no. 3, pp. 3731–3741, 2023, doi:10.1109/TTE.2022.3232560.

[6] M. M. Haque, P. Wolfs, S. Alahakoon, B. C. P. Sturmberg, M. Nadarajah, F. Zare, "DAB Converter With Q Capability for BESS/EV Applications to Allow V2H/V2G Services", *IEEE Transactions on Industry Applications*, vol. 58, no. 1, pp. 468–480, 2022, doi:10.1109/TIA.2021.3123139.

[7] X. Chen, G. Xu, H. Han, D. Liu, Y. Sun, M. Su, "Light-Load Efficiency Enhancement of High-Frequency Dual-Active-Bridge Converter Under SPS Control", *IEEE Transactions on Industrial Electronics*, vol. 68, no. 12, pp. 12941–12946, 2021, doi:10.1109/TIE.2020.3044803.

[8] S. Shao, H. Chen, X. Wu, J. Zhang, K. Sheng, "Circulating Current and ZVS-on of a Dual Active Bridge DC-DC Converter: A Review", *IEEE Access*, vol. 7, pp. 50561–50572, 2019, doi:10.1109/ACCESS.2019.2911009.

[9] X. Liu, Z. Q. Zhu, D. A. Stone, M. P. Foster, W. Q. Chu, I. Urquhart, J. Greenough, "Novel Dual-Phase-Shift Control With Bidirectional Inner Phase Shifts for a Dual-Active-Bridge Converter Having Low Surge Current and Stable Power Control", *IEEE Transactions on Power Electronics*, vol. 32, no. 5, pp. 4095–4106, 2017, doi:10.1109/TPEL.2016.2593939.

[10] F. Lin, X. Zhang, X. Li, C. Sun, W. Cai, Z. Zhang, "Automatic Triple Phase-Shift Modulation for DAB Converter With Minimized Power Loss", *IEEE Transactions on Industry Applications*, vol. 58, no. 3, pp. 3840–3851, 2022, doi:10.1109/TIA.2021.3136501.

[11] R. T. Naayagi, A. J. Forsyth, R. Shuttleworth, "Performance analysis of extended phase-shift control of DAB DC-DC converter for aerospace energy storage system", *in 2015 IEEE 11th International Conference on Power Electronics and Drive Systems*, pp. 514–517, 2015, doi:10.1109/PEDS.2015.7203567.

[12] H. Shi, H. Wen, Y. Hu, L. Jiang, "Reactive Power Minimization in Bidirectional DC–DC Converters Using a Unified-Phasor-Based Particle Swarm Optimization", *IEEE Transactions on Power Electronics*, vol. 33, no. 12, pp. 10990–11006, 2018, doi:10.1109/TPEL.2018.2811711.

[13] H. Wen, W. Xiao, "Bidirectional dual-active-bridge DC-DC converter with triple-phase-shift control", *in 2013 Twenty-Eighth Annual IEEE Applied Power Electronics Conference and Exposition (APEC)*, pp. 1972–1978, 2013, doi:10.1109/APEC.2013.6520565.

[14] J. He, Y. Chen, J. Lin, J. Chen, L. Cheng, Y. Wang, "Review of Modeling, Modulation, and Control Strategies for the Dual-Active-Bridge DC/DC Converter", *Energies*, vol. 16, no. 18, 2023, doi:10.3390/en16186646.

[15] P. Yang, M. Wang, S. Liu, S. Li, X. Chen, Y. Peng, "Unilateral Asymmetric Triple Phase Shift Modulation Strategy for DAB Converter Compromising RMS Current and Soft-Switching Range", *IEEE Transactions on Circuits and Systems II: Express Briefs*, vol. 71, no. 6, pp. 3216–3220, 2024, doi:10.1109/TCSII.2024.3354511.

[16] Y. Xie, R. Ghaemi, J. Sun, J. Freudenberg, "Model Predictive Control for a Full Bridge DC/DC Converter", *IEEE Transactions on Control Systems Technology*, vol. 20, pp. 164–172, 01 2012, doi:10.1109/TCST.2011.2107575.

[17] L. Zheng, R. P. Kandula, K. Kandasamy, D. Divan, "Stacked Low-Inertia Converter or Solid-State Transformer: Modeling and Model Predictive Priority-Shifting Control for Voltage Balance", *IEEE Transactions on Power Electronics*, vol. 36, no. 8, pp. 8934–8952, 2021, doi:10.1109/TPEL.2021.3050115.

[18] Y. Takayama, H. Yamada, "Variable DC-Link Voltage Control of Dual Active Bridge Converter in a Standalone Wind Power Generation System for High-Efficiency Battery-Discharging Operation", *Energies*, vol. 14, p. 6786, 10 2021, doi:10.3390/en14206786.

[19] L. Li, G. Xu, D. Sha, Y. Liu, Y. Sun, M. Su, "Review of Dual-Active-Bridge Converters With Topological Modifications", *IEEE Transac-*

tions on Power Electronics, vol. 38, no. 7, pp. 9046–9076, 2023, doi:10.1109/TPEL.2023.3258418.
[20] C. Suarez Buitrago, D. B. Cobaleda, W. Martinez, "Dual Active Bridge Converter With Variable Transformer for Wide Voltage and Wide Load Range Operation", *IEEE Access*, vol. 11, pp. 90980–90998, 2023, doi:10.1109/ACCESS.2023.3308043.
[21] T. Chen, R. Yu, A. Q. Huang, "Variable-Switching-Frequency Single-Stage Bidirectional GaN AC–DC Converter for the Grid-Tied Battery Energy Storage System", *IEEE Transactions on Industrial Electronics*, vol. 69, no. 11, pp. 10776–10786, 2022, doi:10.1109/TIE.2021.3120483.
[22] H. Fan, H. Li, "High-Frequency Transformer Isolated Bidirectional DC–DC Converter Modules With High Efficiency Over Wide Load Range for 20 kVA Solid-State Transformer", *IEEE Transactions on Power Electronics*, vol. 26, no. 12, pp. 3599–3608, 2011, doi:10.1109/TPEL.2011.2160652.
[23] S. Saeed, J. Garcia, R. Georgious, "Dual-Active-Bridge Isolated DC–DC Converter With Variable Inductor for Wide Load Range Operation", *IEEE Transactions on Power Electronics*, vol. 36, no. 7, pp. 8028–8043, 2021, doi:10.1109/TPEL.2020.3048928.
[24] A. L. Kirsten, F. G. Carloto, T. H. de Oliveira, J. G. P. Roncalio, M. A. D. Costa, "Metodologia de Projeto Generalizada para o Conversor Dab", *Eletrônica de Potência*, vol. 19, no. 3, p. 231–240, Aug. 2014, doi:10.18618/REP.2014.3.231240.
[25] C. G. Marques, J. P. S. Cipriani, M. W. Dickow, L. Roggia, J. R. Tibola, R. Seidel, "Efficiency Enhancement of a Dual Active Bridge Converter with a Variable Inductor for Battery Charging Applications", *in 2024 16th Seminar on Power Electronics and Control (SEPOC)*, pp. 1–6, 2024, doi:10.1109/SEPOC63090.2024.10747469.
[26] S. Saeed, R. Georgious, J. Garcia, "Modeling of Magnetic Elements Including Losses—Application to Variable Inductor", *Energies*, vol. 13, no. 8, 2020, doi:10.3390/en13081865.
[27] W. M. d. Santos, D. C. Martins, "Introdução ao Conversor DAB Monofásico", *Eletrônica de Potência*, vol. 19, no. 1, pp. 36–46, mar 2014, doi:10.18618/REP.2014.1.036046.
[28] Y. Hu, L. Huber, M. M. Jovanović, "Single-Stage, Universal-Input AC/DC LED Driver With Current-Controlled Variable PFC Boost Inductor", *IEEE Transactions on Power Electronics*, vol. 27, no. 3, pp. 1579–1588, 2012, doi:10.1109/TPEL.2010.2082564.
[29] J. M. Alonso, M. Perdigão, M. A. D. Costa, S. Zhang, Y. Wang, "Analysis and experimentation of the quad-U variable inductor for power electronics applications", *IET Power Electronics*, vol. 11, no. 14, pp. 2330–2337, Nov. 2018, doi:10.1049/iet-pel.2018.5076.
[30] S. Saeed, J. García, "Analysis and Validation of a Novel Symmetrical Structure for Toroidal Variable Power Inductors in Energy Storage Systems", *IEEE Journal of Emerging and Selected Topics in Power Electronics*, vol. 12, no. 6, pp. 5915–5929, 2024, doi:10.1109/JESTPE.2024.3445309.
[31] S. Saeed, J. Garcia, M. S. Perdigão, V. S. Costa, B. Baptista, A. M. S. Mendes, "Improved Inductance Calculation in Variable Power Inductors by Adjustment of the Reluctance Model Through Magnetic Path Analysis", *IEEE Transactions on Industry Applications*, vol. 57, no. 2, pp. 1572–1587, 2021, doi:10.1109/TIA.2020.3047593.
[32] J. M. Alonso, M. Perdigão, M. A. Dalla Costa, S. Zhang, Y. Wang, "Variable inductor modeling revisited: The analytical approach", *in 2017 IEEE Energy Conversion Congress and Exposition (ECCE)*, pp. 895–902, 2017, doi:10.1109/ECCE.2017.8095880.
[33] M. S. Perdigão, M. Menke, A. Seidel, R. A. Pinto, J. M. Alonso, "A review on variable inductors and variable transformers: Applications to lighting drivers", *in 2014 IEEE Industry Application Society Annual Meeting*, pp. 1–8, 2014, doi:10.1109/IAS.2014.6978431.
[34] D. Medini, S. Ben-Yaakov, "A current-controlled variable-inductor for high frequency resonant power circuits", *in Proceedings of 1994 IEEE Applied Power Electronics Conference and Exposition - ASPEC'94*, pp. 219–225 vol.1, 1994, doi:10.1109/APEC.1994.316396.
[35] S. Martins, L. Roggia, M. S. Perdigão, R. Seidel, "Planar Magnetic Regulator Applied to an LLC Converter for CCT Control", *IEEE Transactions on Power Electronics*, vol. 39, no. 10, pp. 13300–13308, 2024, doi:10.1109/TPEL.2024.3410232.

BIOGRAPHIES

Conrado Gomes Marques was born in Rio Pardo, RS, Brazil, in 2000. He received the degree in industrial electronics technology and the M.S. degree in electrical engineering from the Federal University of Santa Maria (UFSM), Santa Maria, Brazil, in 2023 and 2025, respectively. He is currently pursuing the Ph.D. degree in electrical engineering at the same university. From March 2025 to December 2025, he was a Substitute Professor with the Colégio Técnico Industrial de Santa Maria (CTISM). His current research interests include electronic control systems and the development of DC–DC converters for battery charging applications.

João Pedro Scherer Cipriani was born in Santa Maria, RS, Brazil, in 1998. He received the B.S. degree in electrical engineering from the Federal University of Santa Maria (UFSM), Santa Maria, Brazil, in 2019, and the M.Sc. degree in electrical engineering from the same university in 2022. He is currently pursuing the Ph.D. degree in electrical engineering in a co-tutelle program between UFSM and the Otto-von-Guericke University Magdeburg (OVGU), Magdeburg, Germany, supported by CAPES. From 2019 to 2020, he was a Research Intern with the Fraunhofer Institute for Integrated Circuits IIS, Dresden, Germany, where he worked on low-power hardware design and energy harvesting systems. His research interests include power electronic converters, control and optimization of energy conversion systems, real-time co-simulation of power system dynamics, and model predictive control applied to power electronic systems.

Leandro Roggia (Member, IEEE) was born in Santa Maria, Brazil, in 1985. He received the B.S.,M.S., and Ph.D. degrees in electrical engineering from the Federal University of Santa Maria, Santa Maria, Brazil, in 2008, 2010, and 2013, respectively. From 2010 to 2013, he was a Professor with Federal Institute of Rio Grande do Sul, Porto Alegre, Brazil. He is currently with the Federal University of Santa Maria, where he is a Professor with the Technical Industrial School of Santa Maria, and a Researcher with Power Electronics and Control Group since 2003, and Electrical and Computational Systems Research and Development Group since 2013. His research interests include power electronics, dc–dc converters, energy storage devices, converters for photovoltaic systems, LED drivers, and power factor correction.

Marina S. Perdigão was born in Coimbra, Portugal, in 1978. She received the M.Sc. and Ph.D. degrees in electrical engineering from the University of Coimbra, Coimbra, Portugal, in 2004 and 2012, respectively. From 2006 to 2012, she conducted her Ph.D. work with the University of Coimbra in cooperation with the University of Oviedo, Oviedo, Spain. Since 2002, she has been with the Polytechnic Institute of Coimbra-Coimbra Institute of Engineering, Coimbra, Portugal, first as a Teaching Assistant and then as an Adjunct Professor, since 2012. She has been a Researcher with the Instituto de Telecomunicações, Coimbra, Portugal, since 2001. She has coauthored of more than 50 journal and conference publications, including more than 20 publications in highly referenced journals. Her research interests include high-frequency switching converters, resonant converters, dc–dc converters, power electronics for renewable energies, IPT, inductor modeling and computer simulation applications. Dr. Perdigão was the recipient of the Best Paper Award of the 2009 IEEE International Symposium on Industrial Electronics and the First Prize Paper, for her technical competence, by the Industrial Lighting and Display Committee of the IEEE Industry Applications Society. She collaborates as a Transactions Paper Reviewer. She is also a Reviewer for other journal publications

Jonas Roberto Tibola was born in Tenente Portela, Brazil, 1988. He received the master's and Ph.D. degrees in electrical engineering from Federal University of Santa Maria (UFSM), Santa Maria, Brazil, in 2013 and 2017, respectively. He worked as a Lecturer with Federal Institute of Education, Venâncio Aires, Brazil, from 2015 to 2016. He is currently with UFSM, where he has been a Professor with Technical and Industrial School of Santa Maria (CTISM). He is also a Researcher with Computational Systems Research and Development Group (GSEC) and Power Electronic Research Group (GEPOC), UFSM. His research interests include modeling, control and instrumentation of pulsewidth modulation (PWM) inverters, PWM modulation strategies, and dc–dc converters.

Álysson Raniere Seidel was born in São Pedro do Sul, Brazil, in 1975. He received the B.S. and Ph.D. degrees in electrical engineering from the Federal University of Santa Maria, Santa Maria, Brazil, in 1999 and 2004, respectively. From 2004 to 2008, he was an Associate Professor with the Department of Electrical Engineering, University of Passo Fundo, Passo Fundo, Brazil. He is currently with Federal University of Santa Maria, where he is a Professor with the Colégio Técnico Industrial de Santa Maria, Santa Maria, Brazil, and a Researcher with the GEDRE/UFSM Intelligence in Lighting research group since 1997, and Electrical and Computational Systems Research and Development Group since 2010. His research interests include power electronics, dc–dc converters, energy storage devices, resonant converters, lighting systems, and self-oscillating systems.